Capacitive tuning of thyristor oscillators enables neuron-like signal amplification

Si En Ng,[1] Nripan Mathews,[1,*] Roberto Fenollosa,[2,†] Jenifer Rubio-Magnieto,[2]
and Juan Bisquert[2,‡]

[1] *School of Materials Science and Engineering, Nanyang Technological University, 50 Nanyang Avenue, Singapore 639798, Singapore*

[2] *Instituto de Tecnología Química (Universitat Politècnica de València-Consejo Superior de Investigaciones Científicas), Camino de Vera s/n, València 46022, Spain*

(Received 31 May 2025; revised 18 October 2025; accepted 4 December 2025; published 3 February 2026)

Self-oscillator devices based on a negative differential resistance (NDR) offer a promising foundation for oscillator-based computing—an emerging computational paradigm that exploits the synchronization, phase dynamics, and collective behavior of coupled nonlinear oscillators for efficient pattern recognition, temporal coding, and signal processing—as well as for implementing spiking neural networks. In this work, we present a compact, thyristor-based two-terminal device that exhibits an ultrasmooth, hysteresis-free NDR response, enabling precise and robust control over complex temporal dynamics. Through a combination of experimental measurements and numerical simulations, we demonstrate that the system supports a tunable Hopf bifurcation, with oscillatory behavior modulated by input current and capacitance. As capacitance increases, the oscillations transition smoothly from sinusoidal to relaxation-type waveforms. The underlying bifurcation structure is analyzed analytically and visualized through dynamical trajectories. Importantly, when operated near the bifurcation threshold, the device exhibits stochastic resonance, amplifying weak periodic signals in the presence of noise, and yielding a 6.8-dB improvement in signal-to-noise ratio. These results establish a neuromorphic-compatible, low-power architecture that bridges nonlinear device physics with functional applications in temporal computation and brain-inspired hardware.

DOI: 10.1103/yhwd-t2wh

I. INTRODUCTION

Neuromorphic circuits draw inspiration from the structure and function of biological neural systems, striving to replicate the brain's efficiency and adaptability in tasks like pattern recognition, sensory processing, and decision-making [1–4]. A key element of these systems is the self-sustained oscillator [5], which is crucial for mimicking the rhythmic and temporal dynamics of biological neural networks. Self-oscillators are nonlinear components or systems that produce periodic signals within electronic circuits using a constant, nonperiodic source of energy. In neuromorphic circuits, oscillators play the role of neurons, to emulate fundamental neural processes, including synchronization, spiking, and rhythmic activity [6].

Spiking neural networks (SNNs) represent a class of neural networks that more closely emulate the way the human brain processes information. Unlike traditional artificial neural networks, which operate using continuous values and compute outputs through weighted sums followed by activation functions, SNNs communicate via discrete electrical pulses—known as spikes—over time. Today, most neural networks are implemented using CMOS (complementary metal oxide semiconductor) technology, which requires complex circuit architectures and a high number of components to simulate spiking behavior [7–10]. Consequently, replicating the dynamic behavior of biological neurons with current fabrication methods remains a significant challenge, resulting in high power consumption and limited efficiency in mimicking brain-like processing.

An additional and growing area is oscillator-based computing [11–13]. This approach uses networks of coupled nonlinear oscillators to perform computation by exploiting their natural dynamics, synchronization patterns, and phase relationships. The collective behavior of these oscillators enables pattern recognition, temporal coding,

*Contact author: nripan@ntu.edu.sg
†Contact author: rfenollo@itq.upv.es
‡Contact author: jbisquer@itq.upv.es

and efficient signal processing. Oscillator-based systems are particularly promising for tasks involving temporal sequences and classification, and they share with neuromorphic hardware the goal of achieving brain-like performance with minimal power consumption [14].

To develop these applications, there is a search for highly compact oscillators that operate without feedback amplifiers [15]. Electrical oscillations have been known for many decades in electronic and in electrochemical systems that contain a negative differential resistance (NDR) [16,17]. This approach consists of connecting a two-terminal nonlinear device with an electrical resistor and a capacitor [18,19], and different types of materials and devices with nonlinear behavior have been explored in this sense in the last few decades. Prominent examples are those of binary oxide memristors such as VO_2 [20,21] endowed with a metal-insulator transition, and organic transistors [22,23]. Advances in neuromorphic photonic systems with laser and nonlinear-optical platforms exhibit neural-like bursting and spiking dynamics [24–26].

Nevertheless, these systems still present important problems, such as stability after moderate cycling times and the difficulty of achieving an equal oscillating frequency for a given set of fabricated devices that would allow further integration in a functional platform.

Here, we consider the use of a thyristor, a robust electronic component that has been known for a long time, as a nonlinear element for the development of simple neuromorphic oscillating systems. While thyristors cannot compete in terms of maximum frequencies, they are competitive in terms of power consumption, oscillation tunability, and relatively low variability; see Table S1 in the Supplemental Material [43], including Refs. [27–32]. Although there are many applications of thyristors as oscillators, they usually form part of a wider CMOS circuit [33]. In contrast, here we show a simple arrangement of a thyristor in parallel with a capacitor and we provide a dynamical model that fully characterizes the Hopf bifurcation with current and capacitance as parameters. We have established a quantitative dynamical model that explains what the conditions are for the emergence of oscillations, i.e., for the Hopf bifurcation. In addition, the model enables control of the frequency and voltage amplitude of the oscillations by the parallel capacitor. We first describe summarily a dynamical system including the components that allow performing simulations, which are compared with experiments, and the stationary current-voltage curve of the standalone thyristor. The excellent agreement between the experimental results and the theory leads us to conclude that thyristor-based spiking neuron oscillators are valuable not only as a testing platform but also as an option for developing applications in neural networks, sensory processing, and machine learning hardware.

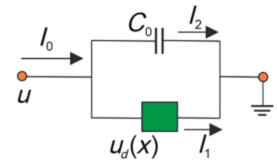

FIG. 1. System inputs and parameters of the oscillatory circuit. $u_d(x)$ represents the nonlinear current-voltage characteristic of the thyristor.

II. DYNAMICAL NEURON MODEL

From a mathematical point of view, certain minimum requirements are necessary to attain oscillations in a dynamical system. Such a system must have at least two interacting variables and an NDR. One of the variables should have fast-destabilizing behavior while the other changes back slowly the system to the previous state [6], exerting in this way a stabilizing effect on the overall dynamics. Together, these components form what is known as a slow-fast dynamical system [34], which is distinguished by the presence of separate timescales. In this context, oscillations often arise suddenly, under a variation of parameters such as the external voltage or the series resistance, in the process of a Hopf bifurcation [35,36].

The standard structure of an oscillator that operates at constant current is shown in Fig. 1 [17–19]. It consists of a nonlinear element (green square) and a capacitor C_0, which enable an oscillatory voltage u when a fixed current I_0 is applied. For operation at constant voltage a series resistance is added [6]. The internal dynamic variable, x, is related to semiconductor equations that describe the complicated transient behavior of thyristors [37,38]. Physically x can be associated with the area of the conducting channel [39]. The voltage u forms the slow variable while x constitutes the fast variable in the oscillatory system.

A key ingredient to build a minimal oscillating system is the conductance function of the nonlinear element. In this regard, we use the following standard approach [40]. Let us introduce a conductance $g(x)$ such that the current in the nonlinear element is

$$I_1 = x = g(x)u. \tag{1}$$

We have

$$g(x) = \frac{x}{u(x)}. \tag{2}$$

Based on this function, a first differential equation is obtained from the addition of currents in Fig. 1:

$$I_0 = C_0 \frac{du}{dt} + g(x)u, \tag{3}$$

which can be written in the standard form [6]

$$\frac{du}{dt} = F = \frac{1}{C_0}[I_0 - g(x)u] \tag{4}$$

in terms of a function $F(u,x)$ that includes the bifurcation parameter I_0. The second equation of the oscillatory model,

$$\frac{dx}{dt} = G = \frac{1}{\tau_k}[g(x)u - x], \tag{5}$$

states the time variation of the internal variable x in terms of τ_k, the relaxation time, and a function $G(u,x)$. Equation (5) introduces a chemical inductor element that is necessary to establish stable oscillations [27,41]. Thus, an electromagnetic inductor, usually present in the "tank circuit" of oscillators [42], is not needed.

An equilibrium point is given by the conditions $\dot{u} = \dot{x} = 0$. For $\dot{u} = F = 0$,

$$\bar{I}_0 = g(\bar{x})\bar{u}. \tag{6}$$

For $\dot{x} = G = 0$,

$$\bar{u} = \frac{\bar{x}}{g(\bar{x})}. \tag{7}$$

In S-type oscillators the function $u_d(I_0)$ obtained from Eqs. (6) and (7) is single valued. The differential resistance is

$$R_d = \frac{du}{dx} = \frac{1 - g'u}{g}, \tag{8}$$

where $g' = dg/dx$. The region of NDR occurs when $g'u > 1$ and the condition $du/dx = 0$ defines the folding points, x_F, of the current-voltage curve. They satisfy

$$g'(x_F)u(x_F) = 1. \tag{9}$$

III. THYRISTOR AND ITS ULTRASMOOTH NDR: MEASUREMENT AND MODEL

A thyristor consists of four alternating doped semiconductor regions forming a p-n-p-n structure [Fig. 2(b)]. It operates as an electronic switch with two stable states, blocking and conduction, and shows an S-type NDR [Fig. 2(a)] [37]. Because of this property, thyristors are widely used in power electronics applications such as ac-dc converters, motor control, and voltage regulation. However, at the same time, this is a key ability for mimicking the firing behavior of biological neurons, which transition between resting and active states. But another element that provides a rebound effect is required. It can be accomplished by a capacitor that charges through the external current, as shown in Figs. 1 and 2(b), and once the voltage across reaches a threshold, the thyristor switches on, allowing the capacitor to discharge rapidly. This sharp voltage drop resembles the action potential of a neuron. Once the current falls below a certain current, the thyristor turns off, and the capacitor begins charging again, leading to a periodic spiking behavior.

The scheme of the thyristor we have used for obtaining oscillations is shown in Fig. 2(b). It is a typical silicon-controlled rectifier (SCR) thyristor (see Experimental methods). Through a resistive gate, the carrier injection into the gate can be gradually controlled and a highly smooth I-V behavior can be obtained. The I-V characteristics of the standalone thyristor used for the experiments are measured galvanostatically, at stationary conditions [line in Fig. 2(c); gate resistance of 150 kΩ]. This measurement is fitted to the following $u_d(x)$ function (Fig. 1 and Fig. S1 in the Supplemental Material [43]) that describes the behavior of a typical thyristor [44]:

$$u_d(x) = R_v x + V_0 \ln\left(\frac{d_0^2 a_0 + d_0 a_1 x + a_2 x^2}{d_0 b_0 + b_{1x} + b_2 x^2}\right) + V_1. \tag{10}$$

Although the fit to the experimental data is not excellent, it is sufficient to build a quantitative dynamical model that describes well the oscillations. A more accurate fitting expression, based on a phenomenological model, is provided in Fig. S2 in the Supplemental Material [43].

In any case, it is obvious, from the shape of the I-V characteristics of Fig. 2(c), that the studied thyristor provides an S-type NDR and it does not show hysteresis in the sense that it yields single values of voltage when measured galvanostatically, no matter the history of the measurement. When the applied voltage is low, the thyristor remains in the blocking state, allowing only a minimal leakage current. This corresponds to the lower branch of the I-V curve, known as the blocking branch. As the voltage increases, the system remains in this state unless a small gate current is applied. This gate current acts as a trigger, causing the thyristor to transition to the conduction state, where a large current flows. This transition occurs rapidly due to internal charge carrier multiplication. In other words, between these two stable states, there is an unstable region in the I-V curve, Eq. (9) [see Fig. 2(d) for the differential resistances], where the system does not stay for a long time. The highly tunable maximum slope provides ample experimental space.

In typical applications, once switched on, a thyristor remains in the conduction state even if the gate current is removed. To turn it off, the applied voltage must be reduced so that the current decreases below a critical level known as the holding current, I_H. Then, the system jumps back to the blocking state. Here, however, we are working at currents well below I_H, which equals 5 mA in this case. Therefore, the thyristor can switch between both states by

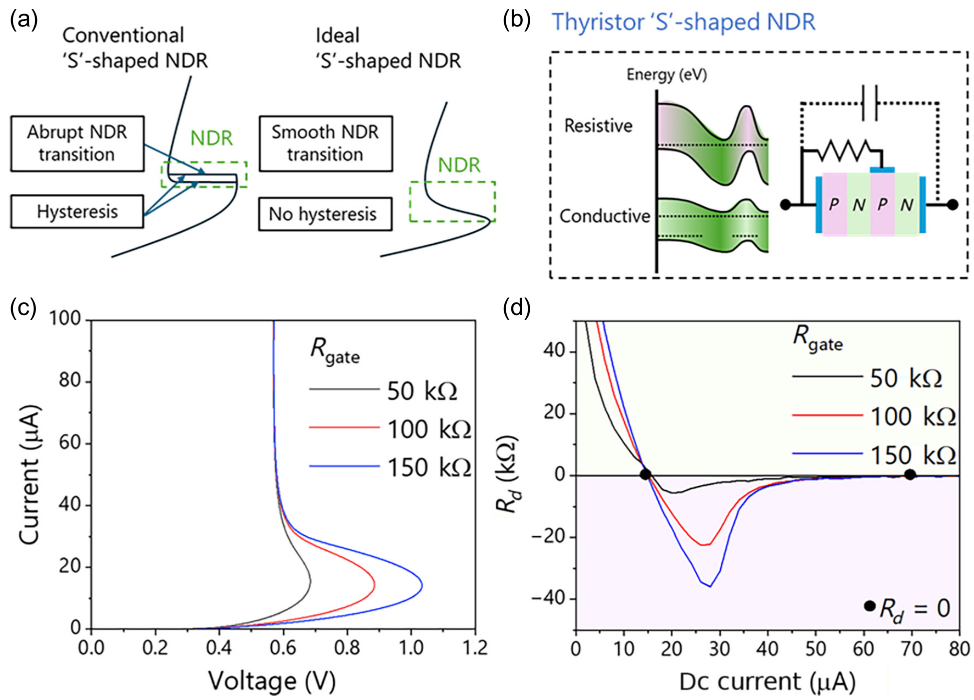

FIG. 2. Current-voltage curve of thyristor-based NDR. (a) A comparison of the features (smoothness and hysteresis) between conventional and an ideal S-shaped NDR. (b) A schematic of the thyristor device architecture and working principle. The electrostatic injection of electronic carriers through a resistive gate ensures smooth and gradual operation. (c) Measured current-voltage curve of the standalone thyristor device (without the parallel capacitor). The profile has continuous slopes and the slopes are highly tunable by changing the gate resistance. (d) The dc resistances where the black circles correspond to the folding points.

the gate current dynamics itself that is in turn enabled by the parallel capacitor.

IV. HOPF BIFURCATION: THEORY-EXPERIMENT ANALYSIS

The bifurcation properties that establish the range of oscillatory domains can be deduced from a linear stability analysis [30,45]. As shown in the Supplemental Material [43], the linear expansion of the dynamical Eqs. (4) and (5) produces the Jacobi matrix J in terms of partial derivatives $F_u, F_x, \ldots$ from which we could obtain the expressions of the trace

$$T_\lambda = F_u + G_x = -\frac{g}{C_0} + \frac{1}{\tau_k}(g'u - 1) \tag{11}$$

and the determinant of J

$$\Delta_\lambda = F_u G_x - F_x G_u = \frac{g}{C_0 \tau_k}\,. \tag{12}$$

With the same oscillatory circuit [see Fig. 3(a)], we explore the response in terms of the output voltage when the input parameters (input current I_0 and parallel capacitance C_0) are varied. Hopf bifurcation occurs when a pair of eigenvalues of J become purely imaginary, i.e., the real part of the eigenvalue changes sign from negative to positive (at $T_\lambda = 0$) by the variation of a parameter [31,32], while the determinant is positive. The bifurcation region with respect to (I_0, C_0) is defined by $T_\lambda = 0$, and limit cycle oscillations occur for $T_\lambda > 0$, as detailed in Fig. 3(b). A first criterion of bifurcation is given by the negative resistance condition $g'u > 1$ indicated above. The value of the capacitor at the bifurcation is

$$C_{0B}(I_0) = \tau_k \frac{g}{g'u - 1}. \tag{13}$$

At the fold points the capacitance $C_{0B} \to \infty$, by Eq. (13).

As illustrated in Fig. 3(b), there is a region characterized by small capacitor values (below the pink line) where the system is stable ($T_\lambda < 0$), i.e., it does not oscillate. When approaching the bifurcation at a fixed current, I_0, from this small capacitor region, damped oscillations are found. Let us define the angular frequency [6]:

$$\omega_0 = \Delta_\lambda^{1/2} = \left(\frac{g}{C_0 \tau_k}\right)^{1/2}. \tag{14}$$

At the Hopf bifurcation, the eigenvalues take the form $\lambda_+ = \pm i\,\omega_0$, and the system produces small-amplitude harmonic oscillations around a stationary point [6], shown

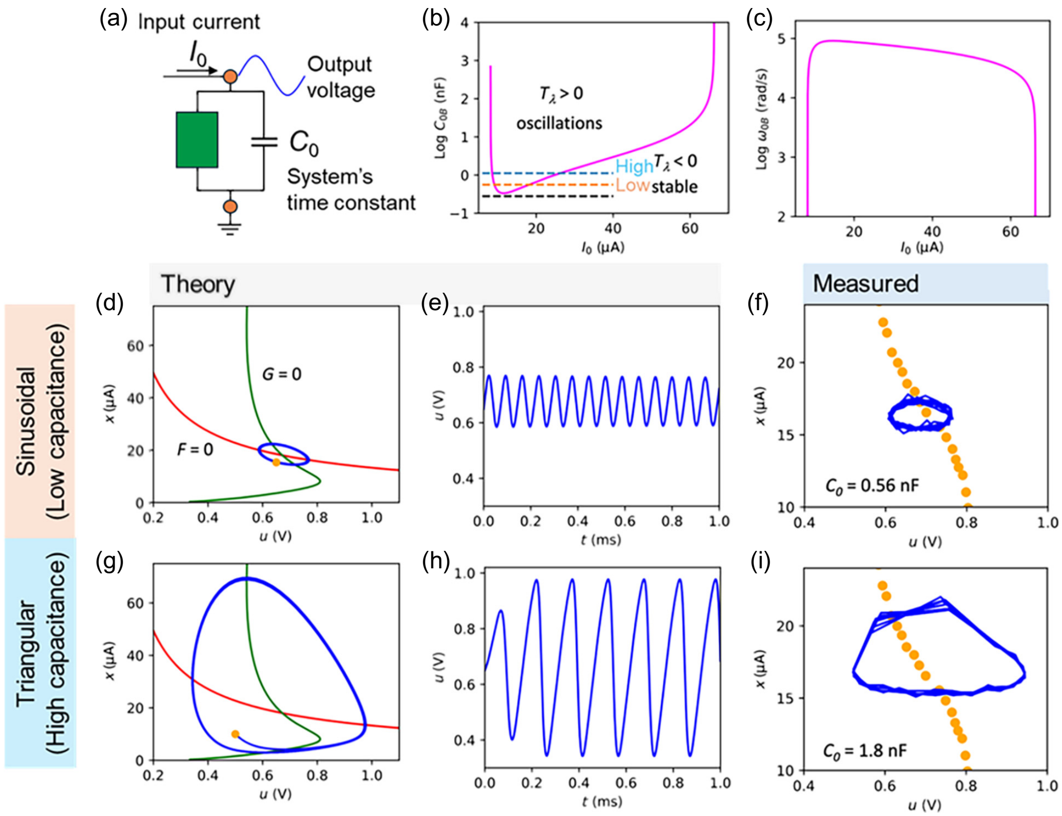

FIG. 3. Response of oscillatory circuit towards system inputs. (a) The system inputs are the current and capacitance of the system; the circuit response is measured by the voltage output. Model calculation of bifurcation properties using the fitted parameters of Fig. 2 and $\tau_k = 6$ μs. (b) Bifurcation diagram of capacitance, C_{0B}, versus current, I_0, and (c) frequency of oscillations at the Hopf bifurcation versus input current. The dashed lines in (b) correspond to the projection lines of constant capacitance through which calculation and measurement of voltage oscillations by sweeping I_0 have been performed in Figs. S2 and S3 in the Supplemental Material [43]. (d),(e) Nullclines and dynamical evolution of the system at constant current $I_0 = 18$ μA and for a capacitance value at the Hopf bifurcation, $C_{0B} = 0.56$ nF. (f) Experimental measurements of current-voltage for input current $I_0 = 18$ mA and a capacitance $C_0 = 0.56$ nF. The orange circles correspond to the stationary I-V curve of the thyristor of Fig. 1(c). (g),(h) Same as (d),(e) but for a much larger capacitance $C_0 = 2$ nF. The orange point is in all cases the starting condition. (i) Same as (f) but for $C_0 = 1.8$ nF.

in Figs. 3(d) and 3(e). The frequency of the oscillations right at the bifurcation is

$$\omega_{0B} = \frac{1}{\tau_k}(g'u - 1)^{1/2}. \tag{15}$$

It is finite for any finite value of C_0, and it coincides with the expression of Eq. (14) at $C_0 = C_{0B}$. We have plotted it in Fig. 3(c). Clearly, the period at the bifurcation is of the order of τ_k, which is estimated as 6 μs in this case, as explained below. To corroborate with theoretical calculations, experimental measurements of the oscillatory circuit are performed. They are realized with very similar parameter values and show, in general, a very good agreement with the theoretical model. In this case, a small capacitance of 0.56 nF is used, and the small-amplitude harmonic oscillations of 170 $\mathrm{mV_{pp}}$ can be observed [see Fig. 3(f)]. The current-voltage phase portrait, shown in Figs. 3(f) and 3(i), corroborates the tendency expected from the simulations. While oscillations do not appear at $C_0 = 0.28$ nF (dashed black line in Fig. S4 in the Supplemental Material [43]), the increase of the capacitance from 0.56 to 1.12 nF widens the current region of oscillations. However, their amplitudes are slightly smaller than those of the simulations due to spatial extension effects not included in our model [46].

If we move away from the bifurcation, at larger capacitor values, the system produces relaxation oscillations of triangular form [47–49], with frequencies much lower than ω_{0B} and larger amplitudes, as shown in Figs. 3(g) and 3(h) [6]. Experimentally, a larger capacitance of 1.8 nF is used, and a highly asymmetric oscillation with large amplitude of 380 $\mathrm{mV_{pp}}$ can be observed [see Fig. 3(i)].

Voltage oscillations can be obtained when sweeping the input current, I_0, at a certain rate. Figure S4 in the Supplemental Material [43] shows this effect for a sweeping rate of 10 μA/s and for two different capacitance values. The color-shaded areas correspond to tight voltage oscillations. Such I_0 sweeping is realized through the dashed lines of

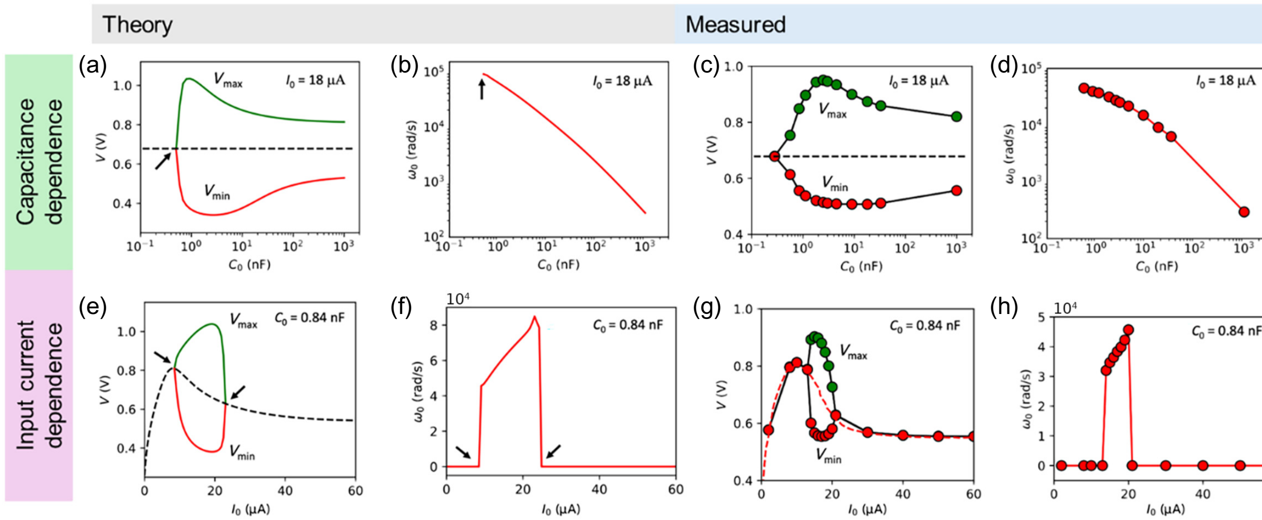

FIG. 4. Amplitude and frequency of oscillations dependent on input parameters. (a) Amplitude and (b) frequency variation with respect to capacitance C_0 of calculated voltage oscillations at a fixed input current $I_0 = 18$ μA. (c),(d) Experimentally measured voltage oscillations with a fixed input current $I_0 = 18$ μA. The dashed lines correspond to the measurements at stationary conditions of the standalone thyristor (without the capacitor in parallel). (e) Amplitude and (f) frequency variation with respect to the input current I_0 at a fixed capacitance $C_0 = 0.84$ nF. The dashed lines correspond to the calculations at stationary conditions of the standalone thyristor (without the capacitor in parallel). The arrows indicate the points where a Hopf bifurcation occurs. (g),(h) Experimentally measured voltage oscillations with a fixed capacitance $C_0 = 0.84$ nF.

Fig. 3(b). The oscillations occur only in the region where $T_\lambda > 0$, between the crossing points with the pink line. They are in fact Hopf bifurcation points and correspond to the blue and orange dots in Fig. S4 in the Supplemental Material [43]. Similarly, this feature is also experimentally observed in Fig. 3 (measured).

A more comprehensive analysis of the oscillatory phenomena is realized by simulating the variation of the amplitude [Figs. 4(a) and 4(e)] and frequency [Figs. 4(b) and 4(f)] of oscillations at different capacitance values and input currents. In general, these features are strongly influenced by the proximity to the Hopf bifurcation points (indicated by arrows) and the value of the capacitor. A key observation here is that close to the bifurcation point, the amplitude of oscillations increases gradually with capacitance [see Fig. 4(a)]. Additionally, in accordance with what we have seen in Fig. 3(c), Fig. 4(b) confirms that oscillations start at a finite frequency value when increasing the capacitance from small values.

However, towards larger capacitance, the amplitude drops with V_{max} and V_{min} saturating to the switching voltage and holding voltage, respectively (see Fig. S5 in the Supplemental Material [43]). Experimentally, this is observed using a constant current of 18 μA [see Figs. 4(c) and 4(d) and Fig. S6 in the Supplemental Material [43]]. By adding a large enough capacitor (200 μF), the system can indeed exhibit relaxation oscillations (see Fig. S7 in the Supplemental Material [43]). Furthermore, a gradual soft threshold can also be observed increasing the input current at a fixed capacitance. Close to the bifurcation point, the amplitude gradually increases [Fig. 4(e)] with increasing input intensity [Fig. 4(f)]. Experimentally, this is observed using a constant capacitance of 0.84 nF [see Figs. 4(g) and 4(h)]. Moreover, for the relaxation oscillators, the frequency of oscillations also decreases linearly with the increase in capacitance. This behavior with saturated amplitude and linear frequency-capacitance relationship is typically observed in reported relaxation oscillators.

In order to infer a meaningful relaxation time, τ_k, that could be applied to the dynamical model, an impedance spectroscopy measurement of the standalone thyristor is undertaken (see Fig. S3 in the Supplemental Material [43]). The impedance spectroscopy result then gives $\omega_k = 2\pi f = 62.8 \times 10^3$ rad/s; hence, $\tau_k = 1/\omega_k = 16$ μs. Being of the same order of magnitude, this value is, however, slightly larger than the value we have used for the simulations, $\tau_k = 6$ μs, which shows a better agreement with more direct experiments, as shown below. A full analysis of the impedance spectra including the influence of other factors such as the presence of a capacitor and the value of the input current is beyond the scope of this paper, and will be presented elsewhere.

Both the measured [see Fig. 4 (measured)] amplitude of the oscillations and their frequency, as a function of the two bifurcation parameters, capacitor and current, show the onset properties of the Hopf bifurcation and the variations predicted by the model shown in Fig. 4 (theory). We have found that the main discrepancy between theory and experiment is the variation of voltage amplitude and

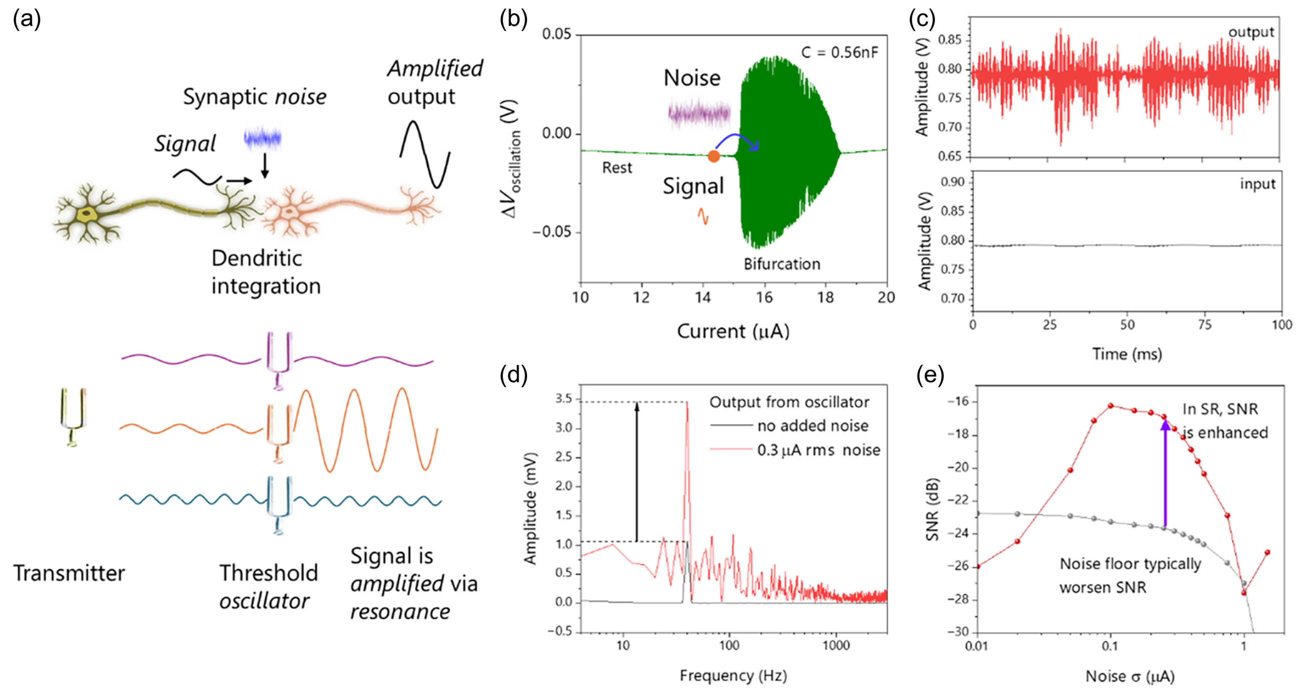

FIG. 5. Amplification of signals via nonlinear addition of noise. (a) Dendrites during neuronal transmission selectively amplify periodic signals while ignoring white synaptic noise. This increases the signal strength while maintaining the signal contrast. (b) Schematic of the bifurcation threshold and the bias point of the signal. Here, a white noise with broadband frequency can be added. (c) The measured 40-Hz signal with and without the 0.3-μA rms white noise of the system biased at 11.8 μA, close to the bifurcation point. (d) The corresponding fast Fourier transform spectrum of the system. (e) Comparison of signal-to-noise ratio for a conventional linear system and a nonlinear stochastic resonance system.

frequency at points very near the Hopf bifurcation [black arrows in Fig. 4 (theory)]. The onset of a Hopf bifurcation can be significantly delayed when system parameters are varied slowly, with the delay influenced by ramp speed, initial conditions, and possible control strategies, particularly in spatially extended systems [46,50,51]. Therefore, the determination of the bifurcation point itself can be very challenging. In fact, the frequency of oscillations in Fig. 4(d) (measured) for the capacitance value that is closest to the bifurcation point, $C_0 = 0.56$ nF, is $\omega_0 = 44.8 \times 10^3$ rad/s, which yields $\tau_k = 6.4$ μs by using Eq. (14), a value slightly smaller than that obtained from the impedance measurements.

As observed in both theory and experimental measurements, the thyristor oscillator shows a relatively gradual increase in oscillation amplitude with increasing input current and the frequency of the oscillations started at a certain finite value. It is interesting to compare this oscillatory behavior with those arising from a different type of bifurcation, for instance, a saddle-node bifurcation on an invariant circle. Here, the frequency of the oscillations can be tuned up to zero, but the amplitude remains practically unchanged [52]. Thus, with regards to amplitude, it yields a kind of all-or-nothing response. These significant differences are important when it comes to the design of a neuromorphic system and the choice of one over the other depends on the specific effect to be achieved. Anyhow, a system like the one we have shown here, with a gradual (or soft) threshold, is expected to allow for graded responses in amplitude, with more sensitivity to small signals, but also less susceptibility to instabilities caused by excessive noise. Graded responses are observed in many biological sensory systems (hair cells in the cochlea and photoreceptors in the retina) [53,54]. Therefore, such graded threshold oscillators can be highly relevant for active signal amplification.

V. SIGNAL AMPLIFICATION VIA STOCHASTIC RESONANCE

Inspired by graded threshold oscillators in the dendrites of neuronal transmission [see Fig. 5(a)] [55], we attempt to mimic the amplification of periodic signals by artificially introducing and modulating the white noise power (controllably by adjusting the rms). Here, we try to showcase how signal strength can be increased while maintaining the signal contrast, which means the improvement in signal-to-noise ratio (SNR) during amplification. This is in contrast to regular inverter amplifiers utilized in the CMOS industry where the noise is also equally amplified.

In this concept known as stochastic resonance, a small alternating current signal (of the order of millivolts) can

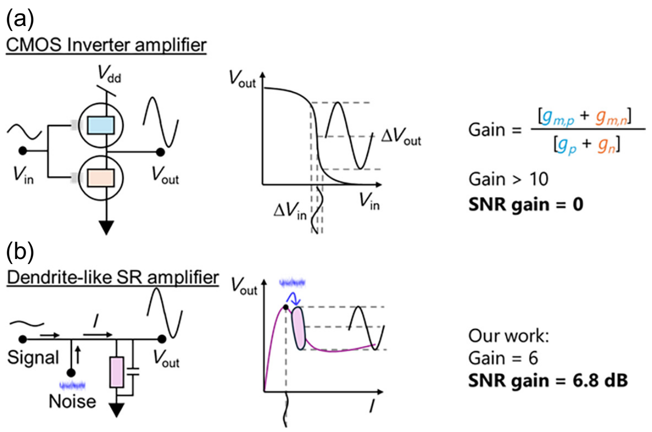

FIG. 6. Signal amplification with SNR gains. (a) Typical CMOS inverter amplifiers have gain of around 10–20. However, the noise is also amplified at the same time, leading to no SNR improvement. (b) Stochastic resonant amplifiers have weaker maximum gain but are capable of amplifying periodic signals as opposed to white noise.

be biased close to the bifurcation point of the oscillator [56]. White noise (broadband frequency introduced by electronic components or intentionally added) can then randomly disturb the signal beyond the bifurcation point and the signal can therefore be amplified [see Fig. 5(b)]. The gold standard for signal amplification would be the inverter amplifier [see Fig. 6(a)], capable of amplifying analog signals with a gain of >10. In contrast to regular inverter amplifiers, stochastic resonant amplifiers [see Fig. 6(b)] can selectively amplify periodic signals as opposed to white (stochastic) noise. This makes SNR gains a much more important parameter than just signal amplitude gain. These dendrite-like amplifiers are much more robust against noise.

To illustrate a typical linear system, the oscillator is biased at 7 μA (far from the bifurcation point) and both the signal and noise are added. The signal is a small oscillatory current (0.1 μA rms with a constant frequency of 40 Hz) while the introduced noise is white noise (0.3 μA rms). The resultant output is therefore a linear addition of both the signal and noise [see Fig. S8(a) in the Supplemental Material [43]] and the corresponding fast Fourier transform spectrum shows the contribution from both the signal and the noise [see Fig. S8(b) in the Supplemental Material [43]]. While not necessarily always the case, the measured 40-Hz signal amplitude is shown to decrease with noise addition. Subsequently, to illustrate a nonlinear system where stochastic resonance is active, the oscillator is biased at 11.8 μA (very close to the bifurcation point). In this case, the same noise results in a crossing over the bifurcation point, and the amplitude is visibly enhanced [see Fig. 5(c)]. While the noise floor is increased, the amplitude of the signal (at 40 Hz) is enhanced more significantly [see Fig. 5(d)].

The white noise itself being randomly distributed adds to the background floor of the signal. As a result, the SNR typically decreases with increasing noise level in a linear system [see Fig. 5(e)]. In this stochastic resonance setup, the nonlinear addition of noise and signal results in an enhancement instead. As a result, the SNR improves by 6.8 dB. When too much noise is added raising the noise floor, the SNR enhancement effect greatly diminishes. However, due to the soft threshold nature [see Fig. S9(a) in the Supplemental Material [43] for a comparison between threshold natures], such a SNR enhancement is highly robust against different bias points [see Fig. S9(b) in the Supplemental Material [43]]. As the bias point is gradually distant from the bifurcation point, the SNR enhancement effect maintains significantly over our negative control (linear system). Eventually, at 11.0 μA, the nonlinear system no longer has any SNR advantage over a linear system at any noise level. In comparison, a relaxation oscillator [see Fig. S9(c) in the Supplemental Material [43]] with a steep threshold nature is much more sensitive to the bias point and therefore demonstrates less robustness for practical purposes. In stochastic resonance, the modulation signal imparts its temporal information to the output signal. This amplification effect is shown to be present in various frequencies of modulation signal (see Fig. S10 in the Supplemental Material [43]).

VI. CONCLUSION

We have shown that a simple electrical circuit consisting of a thyristor and a capacitor in parallel is able to produce stable self-sustained oscillations whose frequency and amplitude can be easily tuned by varying the capacitor. The analysis of the experiments in terms of a dynamical system is a key tool for elucidating the range of parameter values where oscillations occur, as well as critical loci such as Hopf bifurcation points where the system experiences drastic changes in its behavior. Because of their simplicity and stability, and the possibility of controlling the switching frequency, thyristor oscillators represent very promising elements for further development of artificial neuron circuits.

In recent development of oscillators mimicking neuronal components (soma, axon, dendrites), there is an increasing need for high-performance nonlinear components. Here, we also highlight the importance of obtaining very smooth NDR characteristics. With this ideal system, we are able to observe the small-amplitude sinusoidal oscillations and graded thresholding behavior. In biophysical sensing, extremely small signals are often clouded by white noise (being random and having equal power across all frequencies, white noise is conventionally hard to filter). Inspired by biological sensory systems, such noise can be exploited to enhance the detectivity of the small signals. With the graded threshold, we show how oscillatory signals can be actively amplified by white noise. Such an active signal amplification method can be a very useful techniques for high-detectivity sensing of very small signals and highly efficient neuromorphic transmission of signals.

VII. EXPERIMENTAL METHODS

The thyristor used for the experiments is an SCR EC103D from Littelfuse. It has a dc gate trigger voltage and current of 0.8 V and 12 μA, respectively, and a holding current of 5 mA. The anode and gate of the thyristor device (Littelfuse SCR EC103D) are connected with a 150-kΩ resistor, which provides the necessary threshold voltage (0.8 V) for closing the gate. Subsequently, the anode and cathode are taken as the two terminals.

Electrical measurements are carried out under ambient conditions using a Biologic SP-200 potentiostat. In the current sweep measurement, 10 μA/s sweeping rate (1–100 μA) is used and the voltage across the working and counter electrodes is measured.

ACKNOWLEDGMENTS

This work was funded by the European Research Council (ERC) via Horizon Europe Advanced Grant, grant agreement no. 101097688 (“PeroSpiker”). S.E.N and N.M. are grateful for the support from the National Research Foundation (NRF), Singapore, under its Competitive Research Program (CRP) (NRF-CRP25-2020-0002).

DATA AVAILABILITY

The data that support the findings of this article are openly available [57].

[1] D. V. Christensen, *et al.*, 2022 roadmap on neuromorphic computing and engineering, Neuromorph. Comput. Eng. **2**, 022501 (2022).

[2] J. J. Yang, D. B. Strukov, and D. R. Stewart, Memristive devices for computing, Nat. Nanotechnol. **8**, 13 (2013).

[3] Y. Zhang, Z. Wang, J. Zhu, Y. Yang, M. Rao, W. Song, Y. Zhuo, X. Zhang, M. Cui, L. Shen, R. Huang, and J. Joshua Yang, Brain-inspired computing with memristors: Challenges in devices, circuits, and systems, Appl. Phys. Rev. **7**, 011308 (2020).

[4] J. Zhu, T. Zhang, Y. Yang, and R. Huang, A comprehensive review on emerging artificial neuromorphic devices, Appl. Phys. Rev. **7**, 011312 (2020).

[5] A. Jenkins, Self-oscillation, Phys. Rep. **525**, 167 (2013).

[6] J. Bisquert, R. Fenollosa, A. Cordero, and J. R. Torregrosa, Bifurcation and frequency properties of S-type neuronic oscillators, J. Phys. Chem. Lett. **16**, 3616 (2025).

[7] D. Ielmini, Z. Wang, and Y. Liu, Brain-inspired computing via memory device physics, APL Mater. **9**, 050702 (2021).

[8] G. Indiveri, B. Linares-Barranco, R. Legenstein, G. Deligeorgis, and T. Prodromakis, Integration of nanoscale memristor synapses in neuromorphic computing architectures, Nanotechnology **24**, 384010 (2013).

[9] G. Indiveri, *et al.*, Neuromorphic silicon neuron circuits, Front. Neurosc. **5**, 73 (2011).

[10] J. Ahmadi-Farsani, S. Ricci, S. Hashemkhani, D. Ielmini, B. Linares-Barranco, and T. Serrano-Gotarredona, A CMOS–memristor hybrid system for implementing stochastic binary spike timing-dependent plasticity, Philos. Trans. R. Soc., A **380**, 20210018 (2022).

[11] A. Todri-Sanial, C. Delacour, M. Abernot, and F. Sabo, Computing with oscillators from theoretical underpinnings to applications and demonstrators, npj Unconv. Comput. **1**, 14 (2024).

[12] G. Csaba and W. Porod, Coupled oscillators for computing: A review and perspective, Appl. Phys. Rev. **7**, 011302 (2020).

[13] B. Al Beattie, M. Noll, H. Kohlstedt, and K. Ochs, Oscillator-based optimization: design, emulation, and implementation, Eur. Phys. J. B **97**, 7 (2024).

[14] H. W. Kim, S. Jeon, H. Kang, E. Hong, N. Kim, and J. Woo, Understanding rhythmic synchronization of oscillatory neural networks based on NbOx artificial neurons for edge detection, IEEE Trans. Electron Devices **70**, 3031 (2023).

[15] S. Pazos, K. Zhu, M. A. Villena, O. Alharbi, W. Zheng, Y. Shen, Y. Yuan, Y. Ping, and M. Lanza, Synaptic and neural behaviours in a standard silicon transistor, Nature **640**, 69 (2025).

[16] M. T. M. Koper, Oscillations and complex dynamical bifurcations in electrochemical systems, Adv. Chem. Phys. **92**, 161 (1996).

[17] M. Orlik, *Self-Organization in Electrochemical Systems I* (Springer, Berlin, 2012).

[18] A. Wacker and E. Schöll, Criteria for stability in bistable electrical devices with S- or Z-shaped current voltage characteristic, J. Appl. Phys. **78**, 7352 (1995).

[19] P. Maffezzoni, L. Daniel, N. Shukla, S. Datta, and A. Raychowdhury, Modeling and simulation of vanadium dioxide relaxation oscillators, IEEE Trans. Circuits Syst. I Regul. Pap. **62**, 2207 (2015).

[20] A. Todri-Sanial, S. Carapezzi, C. Delacour, M. Abernot, T. Gil, E. Corti, S. F. Karg, J. Nüñez, M. Jiménèz, M. J. Avedillo, and B. Linares-Barranco, How frequency injection locking can train oscillatory neural networks to compute in phase, IEEE Trans. Neural Netw. Learn. Syst. **33**, 1996 (2021).

[21] O. Maher, R. Bernini, N. Harnack, B. Gotsmann, M. Sousa, V. Bragaglia, and S. Karg, Highly reproducible and CMOS-compatible VO_2-based oscillators for brain-inspired computing, Sci. Rep. **14**, 11600 (2024).

[22] P. Belleri, J. Pons i Tarrés, I. McCulloch, P. W. M. Blom, Z. M. Kovács-Vajna, P. Gkoupidenis, and F. Torricelli, Unravelling the operation of organic artificial neurons for neuromorphic bioelectronics, Nat. Commun. **15**, 5350 (2024).

[23] P. C. Harikesh, D. Tu, and S. Fabiano, Organic electrochemical neurons for neuromorphic perception, Nat. Electron. **7**, 525 (2024).

[24] P. R. Prucnal and B. J. Shastri, *Neuromorphic Photonics*, 1st ed. (CRC Press, Boca Raton, 2017).

[25] K. Al-Naimee, F. Marino, M. Ciszak, R. Meucci, and F. T. Arecchi, Chaotic spiking and incomplete homoclinic scenarios in semiconductor lasers with optoelectronic feedback, New J. Phys. **11**, 073022 (2009).

[26] A. Dolcemascolo, A. Miazek, R. Veltz, F. Marino, and S. Barland, Effective low-dimensional dynamics of a mean-field coupled network of slow-fast spiking lasers, Phys. Rev. E **101**, 052208 (2020).

[27] J. Bisquert and A. Guerrero, Chemical inductor, J. Am. Chem. Soc. **144**, 5996 (2022).

[28] J. Bisquert, Negative inductor effects in nonlinear two-dimensional systems. Oscillatory neurons and memristors, Chem. Phys. Rev. **3**, 041305 (2022).

[29] A. Cordero, J. R. Torregrosa, and J. Bisquert, Bifurcation and oscillations in fluidic nanopores: A model neuron for liquid neuromorphic networks, Phys. Rev. Res. **7**, 013282 (2025).

[30] M. W. Hirsch, S. Smale, and R. L. Devaney, *Differential Equations, Dynamical Systems, and an Introduction to Chaos*, 3rd Edition (Academic Press, New York, 2012).

[31] E. S. M. Christopher, P. Fall, John M. Wagner, and John J. Tyson, *Computational Cell Biology* (Springer, Berlin, 2002).

[32] C. Koch and I. Segev, *Methods in Neuronal Modeling, Second Edition: From Ions to Networks* (MIT Press, Cambridge, Mass, 2003).

[33] M. Jotschke, G. Palanisamy, W. Carvajal Ossa, H. Prabakaran, J. Koh, M. Kuhl, W. H. Krautschneider, T. Reich, and C. Mayr, Low-power relaxation oscillator with temperature-compensated thyristor decision elements, Analog Integr. Circ. Signal Process. **116**, 131 (2023).

[34] T. Witelski and M. Bowen, in *Methods of Mathematical Modelling: Continuous Systems and Differential Equations*, edited by T. Witelski, and M. Bowen (Springer International Publishing, Cham, 2015), pp. 201.

[35] P. Strasser, M. Eiswirth, and M. T. M. Koper, Mechanistic classification of electrochemical oscillators—An operational experimental strategy, J. Electroanal. Chem. **478**, 50 (1999).

[36] J. Bisquert, Hopf bifurcations in electrochemical, neuronal, and semiconductor systems analysis by impedance spectroscopy, Appl. Phys. Rev. **9**, 011318 (2022).

[37] G. M. Paolucci, C. M. Compagnoni, N. Castellani, G. Carnevale, P. Fantini, D. Ventrice, A. L. Lacaita, A. S. Spinelli, and A. Benvenuti, Dynamic analysis of current–voltage characteristics of nanoscale gated-thyristors, IEEE Electron Device Lett. **34**, 629 (2013).

[38] J. Cornu and A. A. Jaecklin, Processes at turn-on of thyristors, Solid-State Electron. **18**, 683 (1975).

[39] A. A. Jaecklin, The first dynamic phase at turn-on of a thyristor, IEEE Trans. Electron Devices **23**, 940 (1976).

[40] A. Ascoli, S. Slesazeck, H. Mähne, R. Tetzlaff, and T. Mikolajick, Nonlinear dynamics of a locally-active memristor, IEEE Trans. Circ. Syst. I Regul. Pap. **62**, 1165 (2015).

[41] J. Bisquert, Device physics recipe to make spiking neurons, Chem. Phys. Rev. **4**, 031313 (2023).

[42] I. M. Gottlieb, *Practical Oscillator Handbook* (Newnes, Oxford, 1997).

[43] See Supplemental Material at http://link.aps.org/supplemental/10.1103/yhwd-t2wh for curve fitting, bifurcation conditions, obtaining the relaxation time by impedance spectroscopy, voltage oscillations, relaxation oscillations under very high capacitance, noise measurements, and stochastic resonance.

[44] H. Steinrück, A bifurcation analysis of the one-dimensional steady-state semiconductor device equations, SIAM J. Appl. Math. **49**, 1102 (1989).

[45] J. Guckenheimer and P. Holmes, *Nonlinear Oscillations, Dynamical Systems, and Bifurcations of Vector Fields* (Springer, Berlin, 1983).

[46] M. Kehrt, P. Hövel, V. Flunkert, M. A. Dahlem, P. Rodin, and E. Schöll, Stabilization of complex spatio-temporal dynamics near a subcritical Hopf bifurcationby time-delayed feedback, Eur. Phys. J. B **68**, 557 (2009).

[47] J. Grasman, M. J. W. Jansen, and E. J. M. Veling, in *North-Holland Mathematics Studies*, edited by W. Eckhaus, and E. M. de Jager (North-Holland, Amsterdam, 1978), p. 93.

[48] T. Voglhuber-Brunnmaier and B. Jakoby, Understanding relaxation oscillator circuits using fast-slow system representations, IEEE Access **11**, 99452 (2023).

[49] J. Grasman, in *Mathematics of Complexity and Dynamical Systems*, edited by R. A. Meyers (Springer, New York, New York, NY, 2011), pp. 1475.

[50] S. M. Baer, T. Erneux, and J. Rinzel, The slow passage through a Hopf bifurcation: Delay, memory effects, and resonance, SIAM J. Appl. Math. **49**, 55 (1989).

[51] T. J. Kaper and T. Vo, Delayed loss of stability due to the slow passage through Hopf bifurcations in reaction–diffusion equations, Chaos **28**, 091103 (2018).

[52] L. Ribar and R. Sepulchre, Neuromodulation of neuromorphic circuits, IEEE Trans. Circ. Syst. I Regul. Pap. **66**, 3028 (2019).

[53] K.-H. Ahn, Enhanced signal-to-noise ratios in frog hearing can be achieved through amplitude death, J. R. Soc. Interface **10**, 20130525 (2013).

[54] A. Abtout and J. Reingruber, Analysis of dim-light responses in rod and cone photoreceptors with altered calcium kinetics, J. Math. Biol. **87**, 69 (2023).

[55] A. Gidon, T. A. Zolnik, P. Fidzinski, F. Bolduan, A. Papoutsi, P. Poirazi, M. Holtkamp, I. Vida, and M. E. Larkum, Dendritic action potentials and computation in human layer 2/3 cortical neurons, Science **367**, 83 (2020).

[56] R. Almog, S. Zaitsev, O. Shtempluck, and E. Buks, Signal amplification in a nanomechanical Duffing resonator via stochastic resonance, Appl. Phys. Lett. **90**, 013508 (2007).

[57] N. M. Si En Ng, Roberto Fenollosa, Jenifer Rubio-Magnieto, Juan Bisquert, Dataset for "Capacitive tuning of thyristor oscillators enables neuron-like signal amplification", Zenodo. (2025), https://doi.org/10.5281/zenodo.16810819.